

PROCEEDINGS OF SPIE

SPIDigitalLibrary.org/conference-proceedings-of-spie

Measurement campaign for hyperspectral imaging in complex illumination environments

Steven Golowich, Ronald Lockwood, Richard Nadile, Stuart Biggar, Marius Albota, et al.

Steven Golowich, Ronald Lockwood, Richard Nadile, Stuart Biggar, Marius Albota, Rajan Gurjar, Lin Stowe, Luke Skelly, Ian Fletcher, Ping Fung, Sarah Klein, John Jacobson, Charles Gulley, "Measurement campaign for hyperspectral imaging in complex illumination environments," Proc. SPIE 10644, Algorithms and Technologies for Multispectral, Hyperspectral, and Ultraspectral Imagery XXIV, 106441L (8 May 2018); doi: 10.1117/12.2305200

SPIE.

Event: SPIE Defense + Security, 2018, Orlando, Florida, United States

Measurement campaign for hyperspectral imaging in complex illumination environments

Steven Golowich^a, Ronald Lockwood^a, Richard Nadile^a, Stuart Biggar^b, Marius Albota^a,
Rajan Gurjar^a, Lin Stowe^a, Luke Skelly^a, Ian Fletcher^c, Ping Fung^d, Sarah Klein^a,
John Jacobson^e, and Charles Gulley^f

^aMIT Lincoln Laboratory, Lexington, MA, USA

^bUniversity of Arizona, Tucson, AZ, USA

^cNortheastern University, Boston, MA, USA

^dUniversity of Massachusetts, Amherst, MA, USA

^eNational Air & Space Intelligence Center, OH, USA

^fAir Force LCMC, OH, USA

ABSTRACT

The problem of spectral reflectance retrieval of surfaces via remote hyperspectral imaging is challenging even in benign scenarios, and becomes dramatically more difficult under complex illumination conditions. Shadows, reflections from nearby structures, and atmospheric scattering can all severely impact the observed radiance from ground-level surfaces. In order to study this problem, MIT Lincoln Laboratory recently conducted an airborne data collection experiment that included hyperspectral, laser radar, and pan-chromatic modalities. A comprehensive ground truth data set and extensive efforts directed at sensor characterization makes this data set ideal for the development of hyperspectral exploitation algorithms.

Keywords: Hyperspectral imaging, Ladar imaging, Remote sensing

1. INTRODUCTION

Most current spectral reflectance retrieval methods rely upon the Lambertian assumption and ignore the geometric properties of a scene, greatly simplifying the radiative transfer solution. These approaches work reasonably well in open areas in near nadir viewing but do not accurately retrieve reflectance in shaded regions or when the solar illumination angle with respect to the surface normal or the similar viewing angle are extreme. The accurate surface reflectance retrieval in these situations relies upon an accurate accounting of the local irradiance that can only be accomplished via three-dimensional radiative transfer modeling.^{1,2} Algorithms to accomplish this task, as well as the requirements on collected data, are still in the early stage of development.

In order to study this problem, MIT Lincoln Laboratory (MITLL) recently conducted an experiment in which airborne imagery was collected over an office park in Eastern Massachusetts that included hyperspectral, laser radar, and pan-chromatic modalities. The sensors were co-mounted on MITLL's airborne optical systems testbed (AOSTB),³ a re-configurable sensing system flown on a Twin Otter aircraft. A robust ground operation included placement of reflective tarps and measurement of surface-leaving radiance under a variety of illumination conditions, as well as characterization of the atmosphere via automated solar radiometers and diffuse solar spectral radiance measurements. The comprehensive ground truth data, along with extensive efforts directed at sensor characterization, makes this data set ideal for the development of algorithms to solve various exploitation problems.

This work is sponsored by the Air Force LCMC under Air Force Contract FA8702-15-D-0001. Opinions, interpretations, conclusions, and recommendations are those of the authors and not necessarily endorsed by the United States Government.

Further author information: (Send correspondence to S.G.)

S.G.: E-mail: golowich@ll.mit.edu, Telephone: 1 781 981 0194

R.L.: E-mail: roald.lockwood@ll.mit.edu, Telephone: 1 781 981 1803

2. AIRBORNE MEASUREMENT CAMPAIGN

The measurement campaign consisted of a number of flights over an office park in eastern Massachusetts by a Twin Otter aircraft instrumented with three imaging sensors co-mounted on a common optical bench. The sensors consisted of a hyperspectral imager, a LADAR, and a pan-chromatic camera. An accompanying ground truth collection was also carried out, as will be described in Section 3.

The hyperspectral imager was a whisk-broom scanner covering the 400 to 2500 nm spectral range, based on the COMPASS system.⁴ It employs an Offner-Chrisp spectrometer coupled to a HgCdTe detector array to produce images covering the full VNIR/SWIR range with about 10 nm spectral resolution.

The LADAR system that was flown is part of the AOSTB.³ The laser operates at 1064 nm, and background due to the daytime operation was suppressed through a combination of narrow-band spectral filtering via a bandpass filter and temporal filtering via low duty cycle/short-duration range gate operation. The scanning system utilizes a fast scan mirror (FSM) manufactured by BAE systems. This mirror can be scanned in two axes, which allows for the same fixed region on the ground to be scanned repeatedly during a single aircraft pass, with varying look angle. This mode of operation allowed the ladar to collect returns from the vertical building surfaces as well as the rooftops. The AOSTB is equipped with an Applanix GPS/IMU system.

A FLIR/Point Grey panchromatic 5 megapixel CCD camera was co-mounted on the optical bench with the other two sensors to provide context imagery. The focal length of the lens was chosen to cover a ground area slightly larger than the HSI whisk swath. The context camera was triggered at 1 Hz by the AOSTB Applanix unit.

A Twin-Otter aircraft was selected to host the payload for airborne operations. This platform offers flight endurance in excess of 4 hours at ground speeds as slow as 100 knots and all the necessary on-board space for various research and development activities. Figure 1 shows a picture of MIT-LL's Twin-Otter aircraft on the tarmac at Hanscom Air Force Base (HAFB). The Twin Otter has a 36" x 23" rectangular opening in the belly of the aircraft. A custom optical bench, mounted on four vibration isolators, supported the three imaging sensors and afforded nadir-looking fields of view through the belly hole.



Figure 1: MIT Lincoln Laboratory Twin Otter aircraft.

The flight plans included three different types of aircraft flight passes to acquire the ground targets: 1) flight tracks directly over the center of a target set for viewing directly nadir, 2) flight tracks parallel to but offset from the nadir passes to view the targets at small (6 to 12 degrees) off-nadir angles, and 3) semicircular flight tracks at a stand-off range from the targets with the Twin-Otter in a 30 degree banked turn to allow viewing the sides of building surfaces. A series of passes, each of about 4 minutes duration, were grouped into measurement blocks, which were then combined to build a flight plan for any given day. These flight plans were very successful in ensuring that multiple measurements were taken of the same tarps, from several viewing angles, while the sun elevation and building shadow lines changed during the course of the flight. A typical path for an entire flight is shown in Figure 2.

Part of the rationale for flying the imaging sensors on a common platform was to ease the registration process. The approach taken is to define an HSI camera model with parameters that define the line-of-sight vector with

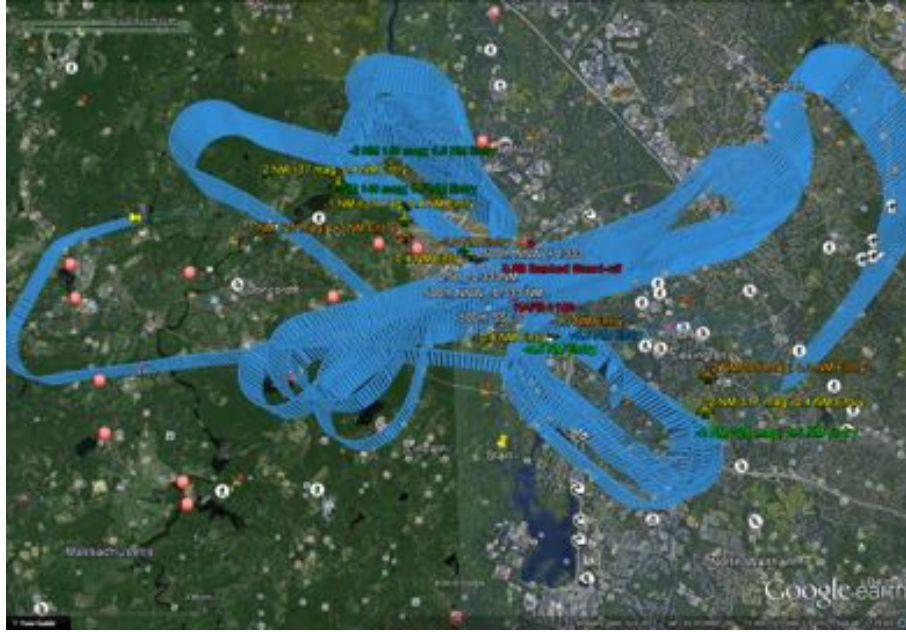


Figure 2: Typical twin otter flight path.

respect to the optical bench as a function of the scan mirror position. The lidar generates a point cloud that is fixed with respect to the optical bench, so the HSI pointing parameters may be adjusted such that the data products are co-registered. In order to carry out this registration in practice, it is desirable to match the HSI image with a temporally coincident lidar image. With such a co-collect, the two sensors will experience the same GPS/INS errors during image formation, thereby minimizing the effects of such drift. We recall that, unlike the HSI sensor, the lidar mirror can be scanned in two axes, which allows for collections in which a fixed region on the ground is scanned in a raster pattern by the lidar as often as possible during a pass. In this mode, the lidar and HSI only observe the same ground swath during the brief interval during which the aircraft is directly over the scene. It is to this lidar image that the HSI image is registered.

3. GROUND TRUTH COLLECTION

The overall objective to accurately characterize and predict reflectance signatures under varying illumination conditions drove the selection of the set of tarps to deploy. Most of these were 3x3 meter red and white type 822 fabric coated tarps from Group 8 Technology Inc. The white tarps have a broadband (400–1600 nm) average reflectance of 57.5%; the red tarps have a peak reflectance of $\sim 72\%$ at 612 nm and less than 2% from 400–500 nm. The selection of contrasting reflectivity between the two tarp types in the blue-green region was intentional to help differentiate between blue sky and sunlit illumination.

Two test sites were chosen that allowed for tarp placements under a variety of illumination conditions. The prime site consisted of a set of six Group 8 tarps (three red and three white) deployed on either side of a three-story office building. The set on the north side was often in the shade, and those on the south side fully sunlit. In addition, several large color tarps (red, blue, and green) were deployed on the north side of the building, far enough away from the building to be sunlit during most of the measurements. Also deployed in the sun on the north side were two large (6 x 6 meter) Group 8 calibration tarps with nominal broadband reflectances of 48% and 2%. Several other 1x1 meter panels were also placed in the scene to aid image and LADAR point cloud registration. Figure 3 shows some ground photos of the target site. Note the shade line on the north side of the building. At the start of each morning flight, all six red and white Group 8 targets were in this shaded region. Near the end of a typical flight, with the Sun elevation close to noon, the shade line would retreat toward the building. An additional nearby site allowed for the deployment of vertically structured targets, and provided a more complex target environment for testing reflectance retrieval algorithms.



Figure 3: Deployed tarps surrounding office building.

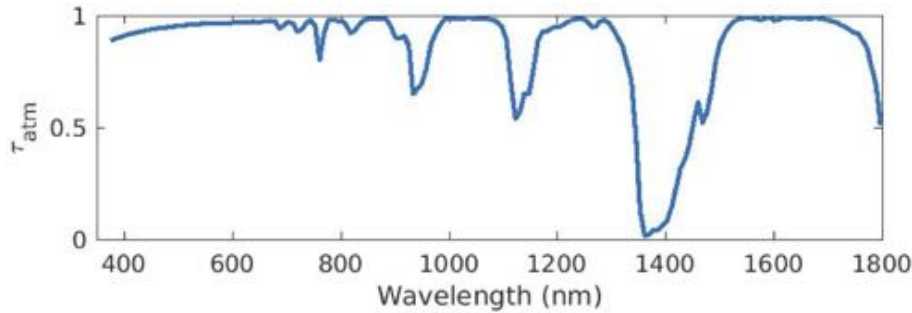
During each flight, a ground measurement team collected in-situ reflectance measurements of each tarp. The upwelling radiance was measured by a calibrated ASD spectroradiometer at eight sample locations of each tarp, and, additionally, that of a Spectralon® panel placed adjacent to the tarp was measured before and after the tarp measurements. The ratio of these spectra yields the reflectance factor of the tarp. The absolute calibration of the ASD is not necessary for the reflectance factor measurement, but it proved to be very useful for data analysis, as will be described in Section 5. Laboratory reflectance measurements were performed as well.

4. ATMOSPHERIC TRUTH COLLECTION

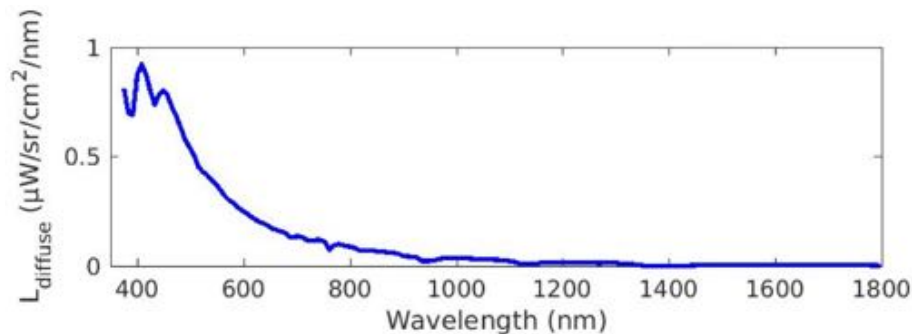
The three-dimensional radiative transfer problem requires that the down-welling radiance at the surface be known in order to model the complex radiative transfer that results from challenging illumination geometries, such as those near buildings and vegetation. The approach taken was to adapt and augment vicarious calibration measurement procedures that quantify atmospheric transmission. The measurements support the quantification of scattering from molecules and aerosols, as well as molecular absorption. The atmospheric measurements are subsequently used to generate atmospheric models, using MODTRAN®, that predict the radiance from the direct solar and diffuse atmospheric components over a range of illumination angles over a given location on the surface.

The measurements utilized two automated solar radiometers (ASRs), one developed by NASA for the AERONET program and manufactured by CIMEL, and the second developed by the Remote Sensing Group (RSG) at the University of Arizona for the Air Force Research Laboratory (AFRL). We will describe the operation of the latter since it was the primary instrument used to develop the atmospheric models.⁵ The RSG ASR is composed of 12 individual co-aligned radiometers that stare directly at the sun with the étendue defined by front and rear apertures that are a fixed distance apart. Following the rear aperture is a narrow-band interference filter and a detector. The band centers are approximately 380, 400, 441, 520, 611, 670, 780, 870, 940, 1030, 1250, and 1550 nm with each having a width of about 10 nm. The bands are carefully chosen to avoid the major atmospheric absorption features, with the exception of the 940 water band used to estimate the water content, in order to derive the aerosol extinction. All but the last two bands utilize silicon photodiodes with the final two using indium gallium arsenide detectors. The field of view of each radiometer is $\pm 2^\circ$. The ASR tracks the sun using a four quadrant detector that is positioned behind a 2 mm aperture and is co-aligned with the radiometers. This enables the sun to be tracked to within $\pm 0.05^\circ$. The sun subtends about 0.5° and is well contained within the field of view of each radiometer. The ASR takes data every two minutes and tracks away from the sun between data acquisitions so that the detectors and filters are not exposed to continuous solar illumination that would reduce their lifetimes.

The ASR data were taken from the roof of a building just northeast of the test sites with measurements initiated shortly after sunrise and continuing until the plane landed and the LADAR/imaging spectrometer measurements were complete for a given day. The data were processed to retrieve the optical depth and MODTRAN® radiative transfer models were successfully generated.⁶ It should be noted that the generation of these models depends upon a stable and cloud free atmosphere. Figure 4 shows examples of the MODTRAN atmospheric transmission and scattering models generated for a particular flight pass and scan number.



(a)



(b)

Figure 4: MODTRAN models for (a) atmospheric transmission, and (b) atmospheric scattering.

The atmospheric models were validated based upon another series of measurements performed simultaneously on the roof of the building. These measurements were taken using a calibrated spectral radiometer manufactured by Analytical Spectral Devices and characterized by the RSG, referred to as the ASD. The spectral radiometer was characterized before and after the measurement campaign and the resulting calibrated radiance data are NIST traceable. The light is fed into the ASD via a fiber optic coupled to a 8° field of view fore optic. The fore optic was mounted in a precision goniometer that was computer controlled to look skyward at various angles. The standardized pattern was to first view a reflectance standard in order to establish the gain settings and then to take a nadir sky view, followed by a series of almucantar views for zenith angles of 30° and 60° and azimuthal angles ranging from 0° , due north, to 360° , again due north, in 45° steps. A final nadir measurement was then taken to complete one measurement cycle with a total of 24 measurements in each series taking about 15 minutes. These measurements were conducted throughout the flight on a given day. A comparison of the MODTRAN® outputs to the ASD measurements are presented in Figure 5.

5. RADIANCE MODELING

We now describe solutions to the forward problem of predicting at-sensor radiance by exploiting all of the ground truth measurements, which is a critical first step toward future development of exploitation algorithms using this data set. Solution of the forward equation of transfer requires a 3-dimensional geometry model of the scene, as well as a model for atmospheric transmittance and scattering. In order to study the spectral aspects of the data without the quality of the geometric reconstruction confounding the results, we have chosen to build high-quality models of the scene by hand, using the open-source modeling tool Blender.⁷ These models were built around the ladar data, ensuring their accuracy, and allowing them to be registered to the hyperspectral imagery using the procedure outlined in Section 2. A Blender model consists of a facetized point cloud, with each facet assigned properties corresponding to its material. With hand-built models, the segmentation of the scene into different materials can be accomplished with high accuracy.

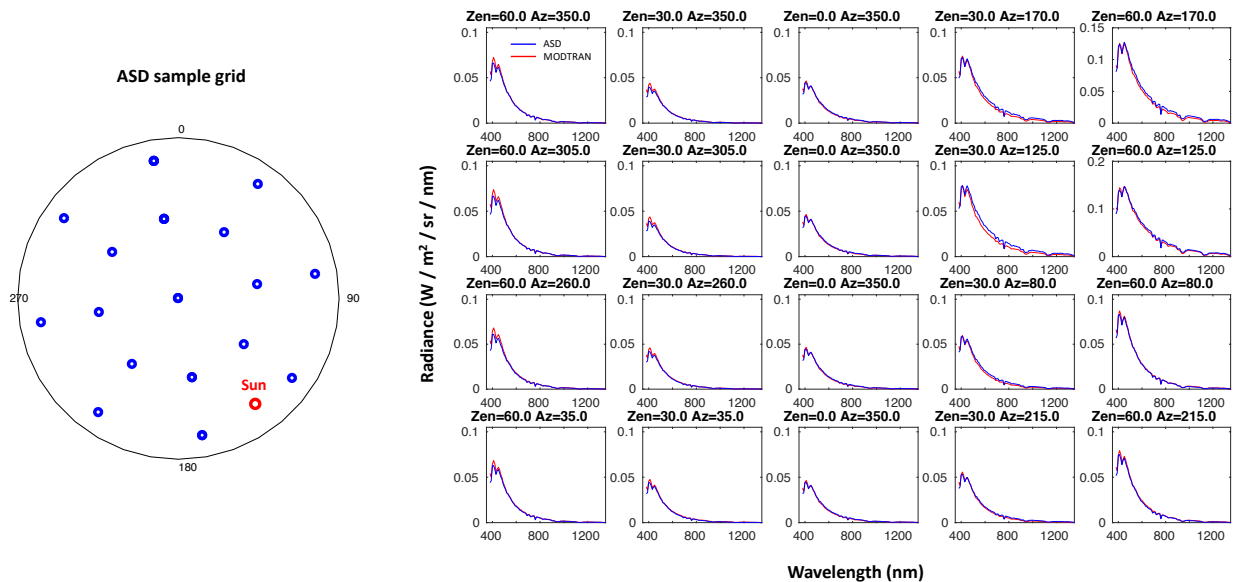


Figure 5: Comparison between diffuse solar radiance predictions (red) and measurements (blue).

A solution to the full equation of transfer can only be done at great computational expense, generally with Monte Carlo integration techniques. Although tremendous progress has been made by the computer graphics community to speed these calculations up, it is still advantageous to incorporate as much special structure about our scenes as possible. In our case, we decouple the atmospheric volumetric scattering and absorption from the surface scattering, and we make simplifying assumptions about the structure of the atmosphere. This decoupling greatly simplifies the solution to each part of the forward modeling calculations, and opens up possibilities for accomplishing the inverse reflectance recovery problem.

The atmosphere-only model makes two idealized approximations: that the atmosphere consists of a number of homogeneous horizontal layers, and that the ground plane is both uniform spatially and Lambertian, although its spectral reflectance may be arbitrary. The first approximation is justified due to the careful selection of flight days with near-pristine weather. A lack of clouds is a necessary condition for the layers to be horizontally homogeneous, and we expect that the aerosol and molecular composition also satisfied this condition, at least locally.

The required outputs of the atmospheric model are the incident radiance distribution at a point on the ground, and the contributions to the radiance at the sensor aperture in its instantaneous field of view. The former consists of direct solar illumination, solar illumination scattered by the atmosphere, and solar illumination reflected by the ground plane and scattered by the atmosphere onto the target. The scattering and reflection processes may occur multiple times, and all paths are subject to transmittance, as dictated by the equation of transfer. An important point about this calculation is that the background reflectance influences the radiance distribution at a point on the ground via scattering processes. Even under very benign weather conditions this adjacency effect can have a measurable impact on observed radiance.

The contributions to the at-aperture radiance consist of surface-leaving radiance modulated by the atmospheric transmittance, plus the path radiance, consisting of light scattered into the sensor IFOV. This latter contribution contains contributions from atmospheric scattering only, as well as scattering in combination with ground reflections (adjacency). Because of our assumption of a spatially uniform ground plane, the relative contributions of different locations on the ground plane are not captured by the calculation. A more complete calculation would include the atmospheric point spread function (PSF), which captures this spatial distribution with non-uniform ground planes.

The calculation of radiative transfer through the atmosphere is performed by the commercial software package MODTRAN®,⁸ which solves the equation of transfer in a horizontally layered atmosphere. The required inputs

are the number and depths of the layers, their molecular compositions, and their aerosol contents. A model for the aerosol scattering is also needed. These inputs are derived from the measurements described in Section 4. MODTRAN® can solve for the light field throughout the atmosphere generated by solar illumination, as well as ancillary quantities such as transmittance. We use MODTRAN® to compute the three necessary inputs to our decoupled solution to the equation of transfer: the diffuse solar radiance distribution at the ground, the direct solar irradiance at the ground, and the atmospheric compensation parameters between the ground and the platform. The result of the diffuse solar radiance is used to assign radiance to an environment map, which is an image indexed by azimuth and zenith angles. An example of such a sky map is shown in Figure 6.



Figure 6: Output of MODTRAN diffuse sky radiance, arranged as a sky map suitable for input to the Mitsuba rendering software.

The solution to the light transport equation is done with Mitsuba,⁹ an open-source physically based rendering code. Mitsuba is capable of performing unbiased spectral rendering, meaning that it can compute a radiometrically correct image given the inputs for illumination, geometry, and scattering. We interact with Mitsuba through the open-source MATLAB interface RenderToolbox,¹⁰ which handles the interface between the Blender 3-d models and Mitsuba, and allows us to manipulate and examine scenes entirely within MATLAB.

Before delving into the modeling results, we will review some facts about the ground targets and truth data from Section 3. The targets that were placed throughout the scene were mainly colored tarps that were chosen to be as Lambertian as possible. In practice, there were several sources of departure from this ideal behavior. For many passes the solar depression angle was quite low, sometimes below 20°. Illumination from such extreme angles tends to lead to non-Lambertian behavior in most materials. Indeed, some preliminary laboratory bidirectional reflectance measurements on two of the deployed tarps confirm that they have a non-trivial BRDF within the range of solar elevation angles encountered in this experiment. Furthermore, the deployed tarps typically exhibited some amount of non-planar creases, folds, scalloping, etc. In combination with glancing illumination, such features give rise to non-uniform irradiance over the surface of the tarp, which, in turn, leads to non-Lambertian apparent BRDF. Finally, the surfaces of the tarps were not uniform due to weathering, and at different times they were covered with varying amount of moisture. Some combination of these effects led to variations in measured reflectance factors.

It is not feasible to capture the details of all of the above effects in the model for the target tarps. Instead, the following approach was taken. We recall from Section 3 that the in-situ ground truth measurements of the tarp consisted of reflectance factors measured with a ratio of nadir-looking ASD spectra of the tarp and a co-located sample of Spectralon®. Multiple (typically eight) spots on each tarp were measured once per flight. As would be expected from the above discussion, these eight reflectance factors often show a large variance. In the calculations, we model the tarps as Lambertian reflectors with reflectance determined by the mean reflectance factor measured on the day of the simulation. The reason this procedure is reasonable is that, by the definition of reflectance factor, the predicted radiant flux from the Lambertian surface, so defined, is equal to that of the measured surface, as long as the collection geometry is unchanged. This latter condition holds to high accuracy for nadir-looking passes that were temporally coincident with the ground truth reflectance factor measurements. We will see below several examples of such coincident measurements. We will also show the consequences of

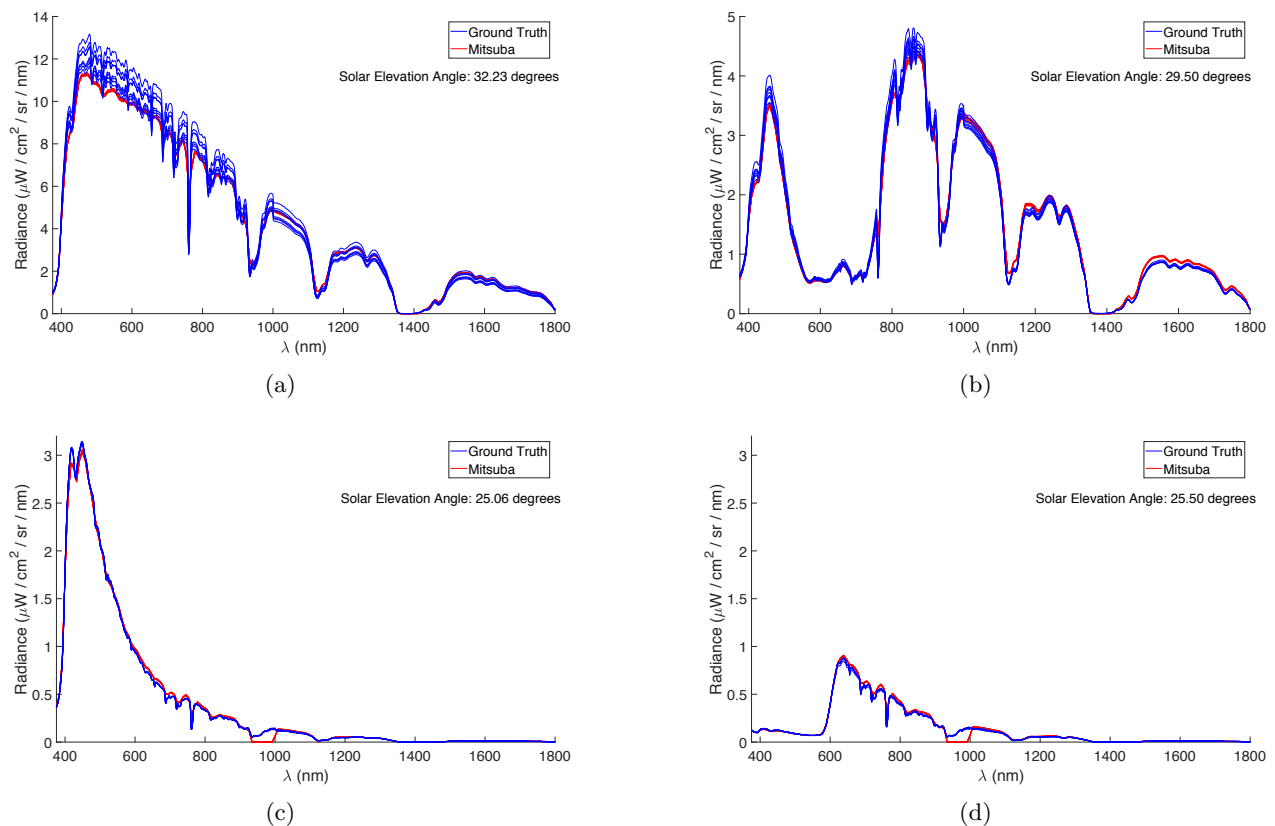


Figure 7: Comparison between measured ground leaving exitant radiance (blue) and forward model predictions (red), for a (a) sunlit 48% reflecting calibration tarp, (b) sunlit blue tarp, (c) shaded white tarp, and (d) shaded red tarp.

violations of this condition, the most extreme of which occurred during banked passes, which were approximately 30° off nadir.

We begin by showing comparisons of predicted and measured ground-leaving radiance, in Figure 7, for both sunlit and shaded tarps. The null between 900-1000 nm in these tarps is an artifact of the reflectance factor measurement. In the sunlit tarp results, we note evidence of drift in the ASD calibration, apparent from the jump in radiance at 1000 nm, that could explain much of the observed discrepancies. We also note that the variance of the eight tarp-leaving measurements is much greater for the sunlit tarps than it is for the shaded ones. This observation supports the hypothesis that much of this variance is due to the surface irregularities of the deployed tarps; such features are much less apparent under diffuse sky, as opposed to direct, sun illumination.

Comparisons between at-aperture radiance and the forward model are shown next. These comparisons offer a more stringent test of the model, due to the additional factors of path radiance due to atmospheric scattering and attenuation between the ground and sensor that come into play. In principle, the HSI PSF plays a role as well, but because our target tarps fill multiple pixels this additional factor does not contribute. We note that, by the discussion above, the apparent reflectance of the tarp may vary with collection time. We only have ground truth measurements of each target once per flight, so there will generally be a mismatch between the time of flight and the ground truth measurement time. Furthermore, we note that the atmosphere model was both developed and validated using radiance measured along paths extending between the ground and top of the atmosphere, and not with paths between the ground and the platform altitude. The vertical distribution of scattering centers is a model assumption, which is a possible source of additional mismatch with the observations.

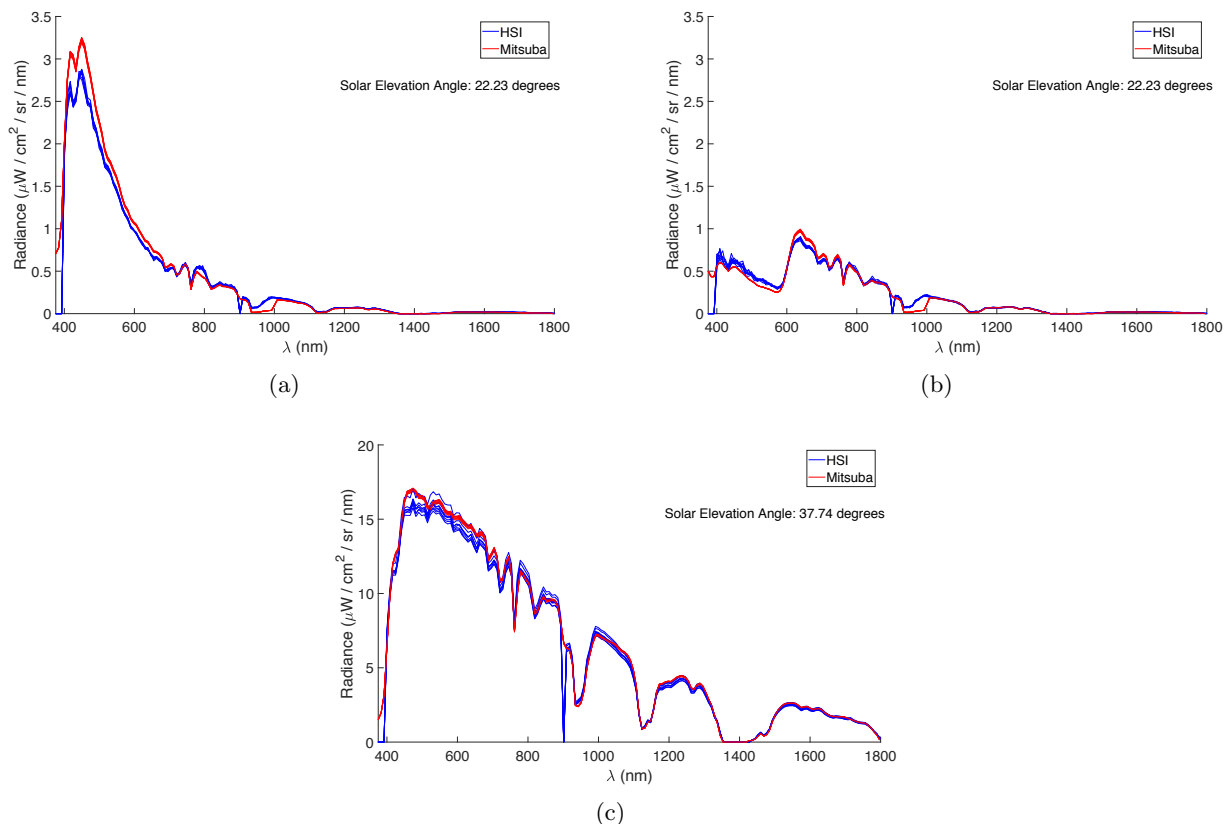


Figure 8: Comparison between at-aperture and forward model predictions of radiance during passes most closely aligned in time with the ground truth reflectance factor measurements; (a) shaded white tarp, (b) shaded red tarp, and (c) sunlit white tarp.

A comparison of observed at-aperture HSI and forward model predictions, in Figure 8, is shown for several tarps observed near to the time at which their ground-truth reflectance factors were measured. We note that the red tarps are essentially opaque below 600 nm, so the observed radiance in this band is essentially all due to atmospheric scattering. There is bias present below 700 nm in these at-aperture results, not observed in Figure 7, which may be the result of HSI calibration uncertainty and/or bias in the atmosphere model. Additional study is required to test these hypotheses.

Figure 9 shows the importance of BRDF on HSI measurements of a blue tarp from different viewing angles. The variation of observed radiance as the viewing angle varies from -12° to $+30^\circ$ off-nadir, in the same plane as the sun, is consistent with a forward-scattering lobe in the BRDF. The low sun elevation angle of around 30° likely contributes to this strong departure from Lambertian behavior.

6. CONCLUSION

Hyperspectral, LADAR, and panchromatic imagers were mounted on a common optical bench and flown on a Twin-Otter aircraft operated by MIT Lincoln Laboratory over a Massachusetts office park on several clear autumn days. Imagery from the sensors was collected and co-registered. An extensive set of in-situ ground truth measurements were made, including surface leaving radiance, surface reflectance, and atmospheric absorption and scattering characterization. Initial three-dimensional radiative transfer modeling results illustrate the utility of this data set for the development of hyperspectral exploitation algorithms.

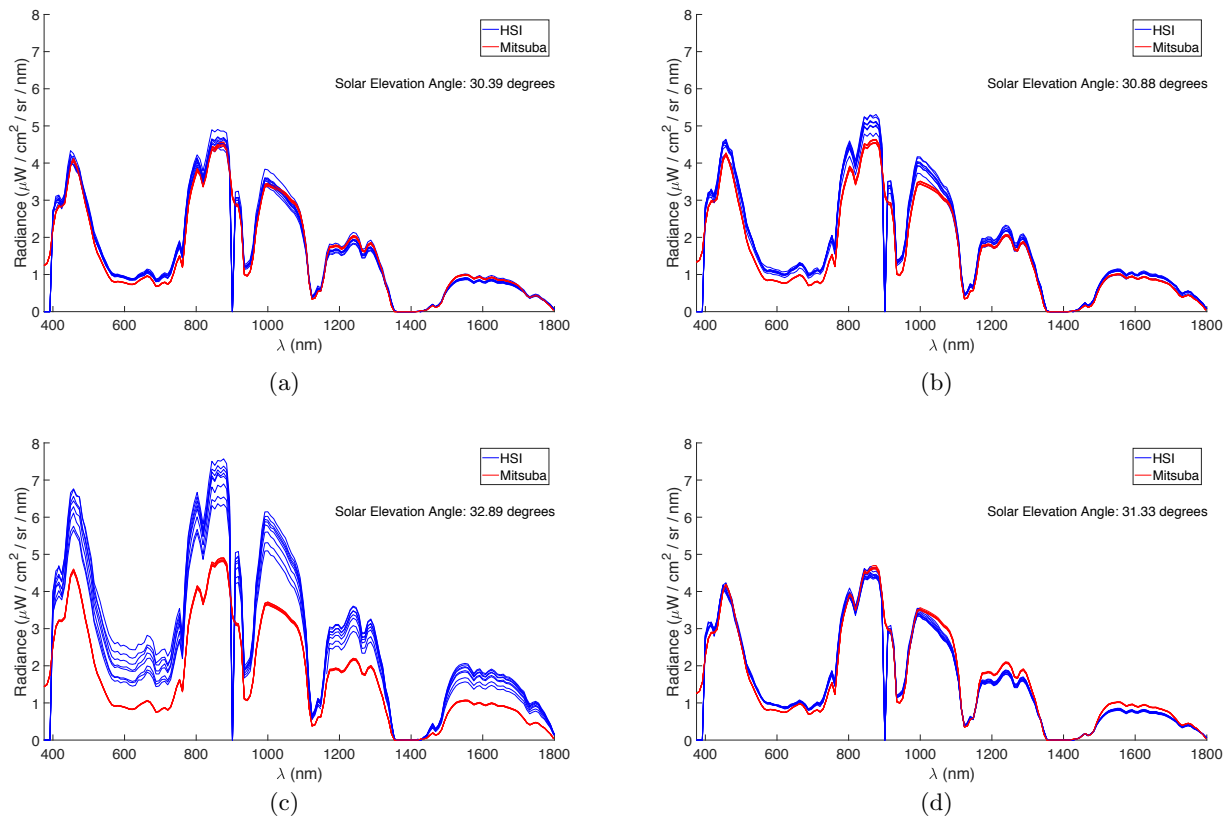


Figure 9: Comparison between at-aperture and forward model radiance predictions of a blue tarp, from viewing angles of (a) nadir, (b) 12° forward off-nadir, (c) 30° forward off-nadir, and (d) 12° backward off-nadir.

REFERENCES

- [1] Borel, C., Ewald, K., Manzardo, M., Wamsley, C., and Jacobson, J., “Adjoint radiosity based algorithms for retrieving target reflectances in urban area shadows,” in [*Proceedings of the 6th EARSeL Imaging Spectroscopy SIG Workshop*], (2009).
- [2] Berger, C., Voltersen, M., Eckardt, R., Eberle, J., Heyer, T., Salepci, N., Hese, S., Schullius, C., Tao, J., Auer, S., Bamler, R., Ewald, K., Gartley, M., Jacobson, J., Buswell, A., Du, Q., and Pacifici, F., “Multi-Modal and Multi-Temporal Data Fusion: Outcome of the 2012 GRSS Data Fusion Contest,” *IEEE Journal of Selected Topics in Applied Earth Observations and Remote Sensing* **6**, 1324–1340 (June 2013).
- [3] Albota, M., Gurjar, R., Mangogna, A., Dumanis, D., and Edwards, B., “The Airborne Optical Systems Testbed (AOSTB).” MSS NATO SET-241 9th NATO Military Sensing Symposium (June 2017).
- [4] Simi, C. G., Winter, E. M., Williams, M. M., and Driscoll, D. C., “Compact Airborne Spectral Sensor (COMPASS),” in [*Proc. SPIE*], **4381**, 129–137, International Society for Optics and Photonics (Aug. 2001).
- [5] Ehsani, A. R., Reagan, J. A., and Erxleben, W. H., “Design and Performance Analysis of an Automated 10-Channel Solar Radiometer Instrument,” *J. Atmos. Oceanic Technol.* **15**, 697–707 (June 1998).
- [6] Biggar, S. F., Gellman, D. I., and Slater, P. N., “Improved evaluation of optical depth components from langley plot data,” *Remote Sensing of Environment* **32**, 91–101 (May 1990).
- [7] “blender.org.” <https://www.blender.org/>.
- [8] Berk, A., Anderson, G. P., Acharya, P. K., Bernstein, L. S., Muratov, L., Lee, J., Fox, M. J., Adler-Golden, S. M., Chetwynd, J. H., Hoke, M. L., et al., “MODTRAN 5: a reformulated atmospheric band model with auxiliary species and practical multiple scattering options,” in [*Proc. SPIE*], **5655**, 88–95 (2004).
- [9] Jakob, W., “Mitsuba - physically based renderer.” <http://www.mitsuba-renderer.org/>.
- [10] Heasly, B. S., Cottaris, N. P., Lichtman, D. P., Xiao, B., and Brainard, D. H., “RenderToolbox3: MATLAB tools that facilitate physically based stimulus rendering for vision research,” *Journal of Vision* **14**, 6–6 (Feb. 2014).